Magnetic graphene oxide modified by chloride imidazole ionic liquid for the high-efficiency adsorption of anionic dyes†

Huan Wang[ab] and Yinmao Wei[*a]

Magnetic graphene oxide modified with 1-amine-3-methyl imidazole chloride ionic liquid (LI-MGO) was prepared through chemical co-precipitation and modified using 1-amine-3-imidazolium chloride ionic liquid. The as-prepared LI-MGO was characterized using X-ray diffraction (XRD), transmission electron microscopy (TEM) and Fourier transform infrared spectrometry (FT-IR). The adsorption properties were evaluated through adsorption experiments with two kinds of anionic dyes, orange IV (OIV) and glenn black R (GR) and two kinds of cationic dyes, acridine orange (AO) and crystal violet (CV). The results indicated that the adsorption data fitted the Langmuir isotherm and followed pseudo-second-order kinetics. The maximum adsorption capacities for GR, OIV, AO and CV were 588.24, 57.37, 132.80 and 69.44 mg g^{-1} at 298 K, respectively. LI-MGO has better selective adsorption for anionic dyes than magnetic graphene oxide (MGO) due to electrostatic interactions. Moreover, the LI-MGO adsorbent can be magnetic separated and is easy to prepare. It demonstrated that LI-MGO would have great potential as an efficient environmentally friendly adsorbent for the removal of anionic dyes in water treatment.

1 Introduction

Organic dye wastewater discharged from industrial coloring and printing processes has many detrimental effects on the environment and human health.[1] With better awareness of these problems, a number of techniques to remove dyes have been employed to treat wastewater, including degradation,[2] electrochemical treatment,[3] reverse osmosis,[4] ion exchange, and adsorption.[5,6] Among these methods, adsorption is believed to be the most effective way to remove dye from wastewater.[7] Various adsorbents have been reported to remove dye from wastewater in the literature, such as clay minerals,[8] oxides,[9] zeolites[10] and carbon materials.[11,12] However, the performance of these materials is limited by their relatively low densities of surface functional groups.[13] Graphene oxide, as a kind of carbon material, has attracted much attention as a potential adsorbent due to its high specific surface area and its ease of surface functionalization,[14,15] which contains a large number of carboxyl, ketone, epoxy and hydroxyl groups on its surface.[16] However, graphene oxide is usually collected through high-

speed centrifugation, which increases the operational cost for its practical application.[17] To overcome the challenges of its difficulty of separation, Fe_3O_4 magnetic nanoparticles have been increasingly utilized in magnetic separation, due to their distinguished magnetic properties.[18,19]

Recently, graphene oxide[20] and its hybrids were successfully synthesized with β-cyclodextrin and acrylic acid,[21,22] metal oxides,[23,24] 4-aminothiophenol and 3-aminopropyltriethoxysilane,[25] and tripolyphosphate[26] to remove cationic dyes in wastewater, and showed enhanced adsorption properties because they combine the advantages of graphene oxide and functional groups. However, Ramesha et al.[27] reported that graphene oxide showed removal efficiencies of up to 95% for cationic dyes, while the adsorption of anionic dyes was negligible, because the large negative charge density available in aqueous solutions helps the effective adsorption of cationic dyes on graphene oxide. Adsorbents for anionic dyes are usually surface cationic modified materials such as cationic surfactant hexadecylpyridinium bromide modified peanut shell,[28] surfactant modified coir pith,[29] cationic surfactant modified wheat straw,[30] cationically modified orange peel powder[31] and quaternary ammonium salt modified chitosan magnetic composites.[32] But the adsorption capacity for anionic dyes on these adsorbents is lower. So there is an urgent need for the design of novel functional adsorbents for the efficient adsorption of anionic dyes. Changing the surface charge of graphene oxide through chemical modification is an important way to improve the effective adsorption of anionic dyes.

As a potential environmentally-friendly solvent, room temperature ionic liquids (ILs) are receiving much attention

[a]Key Laboratory of Synthetic and Natural Function Molecule Chemistry of Ministry of Education, College of Chemistry & Materials Science, Northwest University, Xi'an 710069, China. E-mail: ymwei@nwu.edu.cn; Fax: +86-29-88302604; Tel: +86-29-88302604

[b]College of Chemistry and Chemical Engineering, Xianyang Normal College, Xianyang 712000, China

† Electronic supplementary information (ESI) available. See DOI: 10.1039/c6ra27530c

owing to their numerous advantages over conventional solvents, such as their good dissolving ability, recyclability, low volatility, non-flammability, high thermal and chemical stabilities, and high ionic conductivity.[33,34] They have also been successfully applied in the areas of the separation of 2-phenyl-ethanol,[35] gas separation,[36] and the recoveries of solvents[37] and electrolytes in sensitized solar cells.[38] Chen *et al.*[39] has immobilized ammonium ionic liquids on LDHs to improve the adsorption properties for reactive orange 5. Liu *et al.*[40] reported that a hyperbranched polymeric ionic liquid (hb-PIm$^+$PF^{6-}) with imidazolium backbones has been synthesized and it exhibited high adsorption capacity toward anionic dyes. An imidazolium-salt based IL containing nitrogen atoms can facilitate a high atomic percentage of nitrogen as a functional solvent due to the presence of more nitrogen atoms, which can further change the surface charge of the material.

Herein, novel LI-MGO nanocomposites were designed directly from MGO and chloride imidazole ionic liquid. In this paper, we introduced Fe_3O_4 nanoparticles to synthesize MGO through chemical co-precipitation, and then we utilized a chloride imidazole ionic liquid as a functional solvent to modify MGO, to prepare MGO-IL. The introduction of the Fe_3O_4 nanoparticles could well solve the difficulty of separation, and the IL not only increased the water-solubility of the composite but also could change the functional groups on the surface of MGO. MGO and LI-MGO were used for the adsorption of two anionic dyes and two cationic dyes from simulated wastewater with fast magnetic separation. The effects of treatment time, initial concentration and pH value on the dye adsorption capacity of the prepared LI-MGO are investigated. The adsorption kinetics and adsorption isotherms are also investigated by fitting the experimental data with different models and an adsorption mechanism is proposed. LI-MGO is found to possess a unique capability to remove anionic dyes very quickly and efficiently from wastewater.

2   Experimental section

2.1   Experimental reagents

Flake graphite (99.95%) was supplied by Qingdao Chenyang Graphite Co., Ltd. (Qingdao, China). Ferric chloride hexahydrate and ferrous chloride tetrahydrate were purchased from the National Medicine Group Chemical Reagent Co., Ltd. (Shanghai, China). Acridine orange (AO), crystal violet (CV), orange IV (OIV), glenn black R (GR), 1-methylimidazole and 1-amino-3-chloropropane hydrochloride were purchased from the Aladdin Chemical Reagent Co., Ltd. (Shanghai, China). The other reagents were of analytical grade.

2.2   Preparation of adsorbents

2.2.1   Synthesis of 1-amine-3-methyl imidazole chloride. 1-Amine-3-methyl imidazole chloride was prepared according to a process reported in the literature.[41] 35.9690 g of 1-methyl-imidazole (0.4381 mol) and 59.9630 g of 1-amino-3-chloropropane hydrochloride (0.4381 mol) were added to a 250 mL three-necked flask and dispersed in 50 mL of anhydrous

methanol. The mixture was stirred at 80 °C for 48 h. The reaction mixture was evaporated to remove any methanol after cooling to room temperature. A white solid was obtained after placing in a refrigerator for 12 h, and then the supernatant was poured out. The white solid was washed three times with anhydrous alcohol, which was filtered and evaporated to remove any ethanol. Then a potassium hydroxide methanol solution was added to the obtained white solid dissolved in methanol, and the pH was adjusted to 8.0, and this was evaporated to remove the ethanol and water. The product was dissolved in methanol, filtered to remove any potassium chloride and evaporated to remove any methanol again. Finally, the product was dried in a vacuum oven at 60 °C to obtain 1-amine-3-methyl imidazole chloride (LI).

2.2.2   Preparation of LI-GO. GO was prepared from flake graphite powder using a modified Hummers–Offeman method[42] and was then used as a starting material for the functionalization of GO. Firstly, 0.2 g of GO was added to 85 mL of thionyl chloride in a 250 mL three-necked flask and the mixture was ultrasonicated for 30 min to exfoliate the GO sheets. Then 4 mL of *N,N*-dimethylformamide was added as catalyst and the mixture was refluxed at 70 °C for 8 h. Finally, the product was filtered and washed with deionized water. Then the product was dried in a vacuum oven at 60 °C. The acyl chloride graphite obtained and 0.4 mL of LI was added to 100 mL of *N,N*-dimethylformamide and the mixture was refluxed at 80 °C for 31 h. The product was filtered and washed with deionized water, and then the product was dried in a vacuum oven at 60 °C to obtain 1-amine-3-methyl imidazole chloride-functionalized GO (LI-GO).

2.2.3   Preparation of MGO and LI-MGO. LI-MGO was obtained through the co-precipitation method with LI-GO and Fe^{3+} ($FeCl_3 \cdot 6H_2O$) and Fe^{2+} ($FeCl_2 \cdot 4H_2O$) salts in an alkaline medium. Briefly, 2.3245 g of $FeCl_3 \cdot 6H_2O$ and 0.8549 g of $FeCl_2 \cdot 4H_2O$ were dissolved in 30 mL of distilled water, which was purged under a N_2 flow (30 mL min^{-1}) for 30 min. Then 0.2 g of LI-GO was ultrasonicated for 1 h ahead and was dropped at a rate of 10 mL min^{-1}. The mixture was heated to 60 °C and quickly dropped into ammonia to adjust the pH of the solution to 11.0. The solution was stirred continuously for 2 h at 60 °C. The obtained product was magnetically separated and washed to neutral with distilled water. Finally it was dried under vacuum at 60 °C, and the ground product is referred to as LI-MGO. MGO was also prepared using similar steps, only LI-GO was replaced with GO.

2.3   Characterization of LI-MGO

^{1}H NMR spectra of LI were obtained using an AV600 high resolution nuclear magnetic resonance spectrometer (Bruker, Germany). Transmission electron microscopy (TEM) images of MGO and LI-MGO were recorded using an H-600 electron microscope (Hitachi, Japan). Fourier transform infrared (FT-IR) spectra were obtained using a Nicolet iS10 FT-IR spectrophotometer (Thermo Fisher Scientific, USA). Wide-angle (5–70°, 40 kV/30 mA) powder X-ray diffraction (XRD) measurements were carried out using a D2 PHASER X-ray diffractometer (Bruker, Germany). The specific surface area and gas adsorption

isotherms of the sample were measured using N_2 physisorption measurements on an ASAP 2020C (Micromeritics, USA). Zeta potentials were measured on a Zetasizer Nano Series (Malvern, Britain).

2.4 Adsorption experiments

OIV and GR were chosen as the model of anionic dyes for dye adsorption studies, while AO and CV were chosen as the model of cationic dyes. The chemical structures of the four dyes are shown in Fig. 1. The adsorption processes for the dyes (initial concentration: 40 mg L^{-1}) onto MGO and LI-MGO were carried out at the optimum pH and at different temperatures (4, 25, and 45 °C) in aqueous media. A sample of 0.01 g of MGO or LI-MGO was added to a conical flask with 25 mL of dye solution, and the mixture was shaken in a shaker for 12 h. Then the mixture was separated using a magnet and the final concentration of OIV, GR, AO and CV was determined using a UV-Vis spectrophotometer (SPECORD 50 PLUS, Analytikjena, Germany) at 440 nm, 520 nm, 490 nm and 580 nm, respectively. Similarly, the kinetics of adsorption were also measured at different dye concentrations (GR and AO: 20, 40, 60, 80, 100, and 120 mg L^{-1}, and OIV and CV: 2, 4, 8, 12, 16, 20, 24, and 30 mg L^{-1}) at the optimum pH and at different temperatures (4, 25, and 45 °C). The adsorption capacities for dyes adsorbed onto MG or LI-MGO were determined according the following eqn (1):

$$q_t = \frac{(C_0 - C_t) \times V}{m} \tag{1}$$

where C_0 and C_t are the initial and temporary concentrations of the dye (mg L^{-1}), respectively, and m is the weight of the adsorbent (g).

The effect of pH on the adsorption performance was measured over the pH range of 2–10 at 25 °C. The desired pH of the solution was adjusted by adding Britton–Robinson buffer solution.

3 Results and discussion

3.1 Preparation and characterization of LI-MGO

Fig. 2 shows a ^{1}H NMR spectrum of 1-amine-3-methyl imidazole chloride. The H atoms annotated in the chemical structure of 1-amine-3-methyl imidazole chloride can be found in Fig. 2. This shows that 1-amine-3-methyl imidazole chloride was synthesized successfully. The synthesis steps of 1-amine-3-methyl imidazole chloride-functionalized MGO are shown in Fig. 3. The synthesis steps of 1-amine-3-methyl imidazole chloride-functionalized MGO are divided into two stages. Firstly, because the surface of graphene oxide contains a large number of carboxyl groups, the carboxyl groups on the surface of graphene oxide reacted with dichloro-sulfoxide to produce acyl chloride groups, which then reacted with the 1-amino-3-methyl imidazole chloride ionic liquid that was synthesized to produce 1-amine-3-methyl imidazole chloride-functionalized GO. In the second step, Fe^{3+} and Fe^{2+} were used as ion sources and 1-amine-3-methyl imidazole chloride-functionalized MGO was synthesized through chemical co-precipitation over the pH range of 11–12.

TEM images of MGO and LI-MGO are presented in Fig. 4. The TEM image of MGO shows that the Fe_3O_4 nanoparticle distribution is uniform and that they have an average particle size of 10 nm (Fig. 4a). Fig. 4b reveals that the Fe_3O_4 nanoparticles on LI-MGO are larger compared to those on MGO and are present in a layer on the surface of GO. This phenomenon is due to magnetic attraction and the huge nanoparticle surface energy (100 dyn cm^{-1}) of the Fe_3O_4 nanoparticles, so the Fe_3O_4 nanoparticles easily undergo particle agglomeration during the coprecipitation process of LI-GO with Fe^{2+} and Fe^{3+}. After GO was functionalized with 1-amino-3-methyl imidazole chloride ionic liquid, it can be seen clearly that LI-MGO has a much rougher surface than MGO. The TEM images show that LI-MGO was fabricated successfully.

Fig. 5 shows FT-IR spectra of LI, MGO and LI-MGO. The peak shown by MGO and LI-MGO at 3440 cm^{-1} corresponds to the
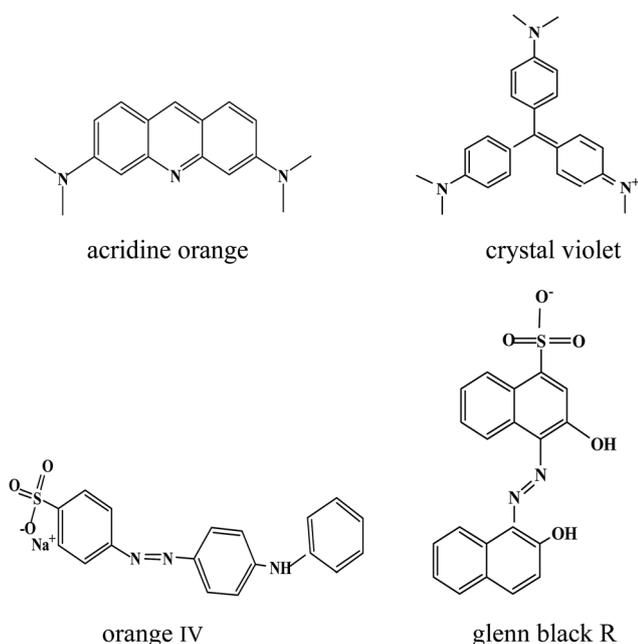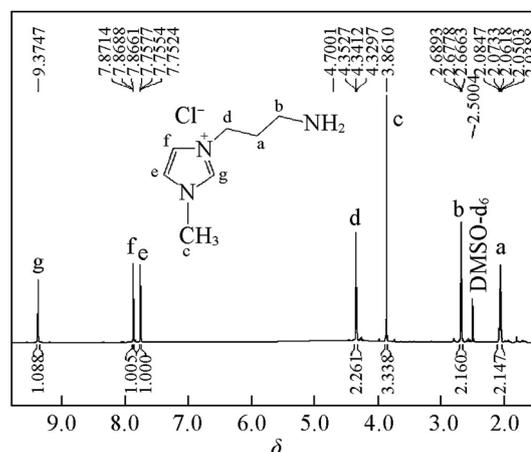

Fig. 1 Chemical structure of dyes.

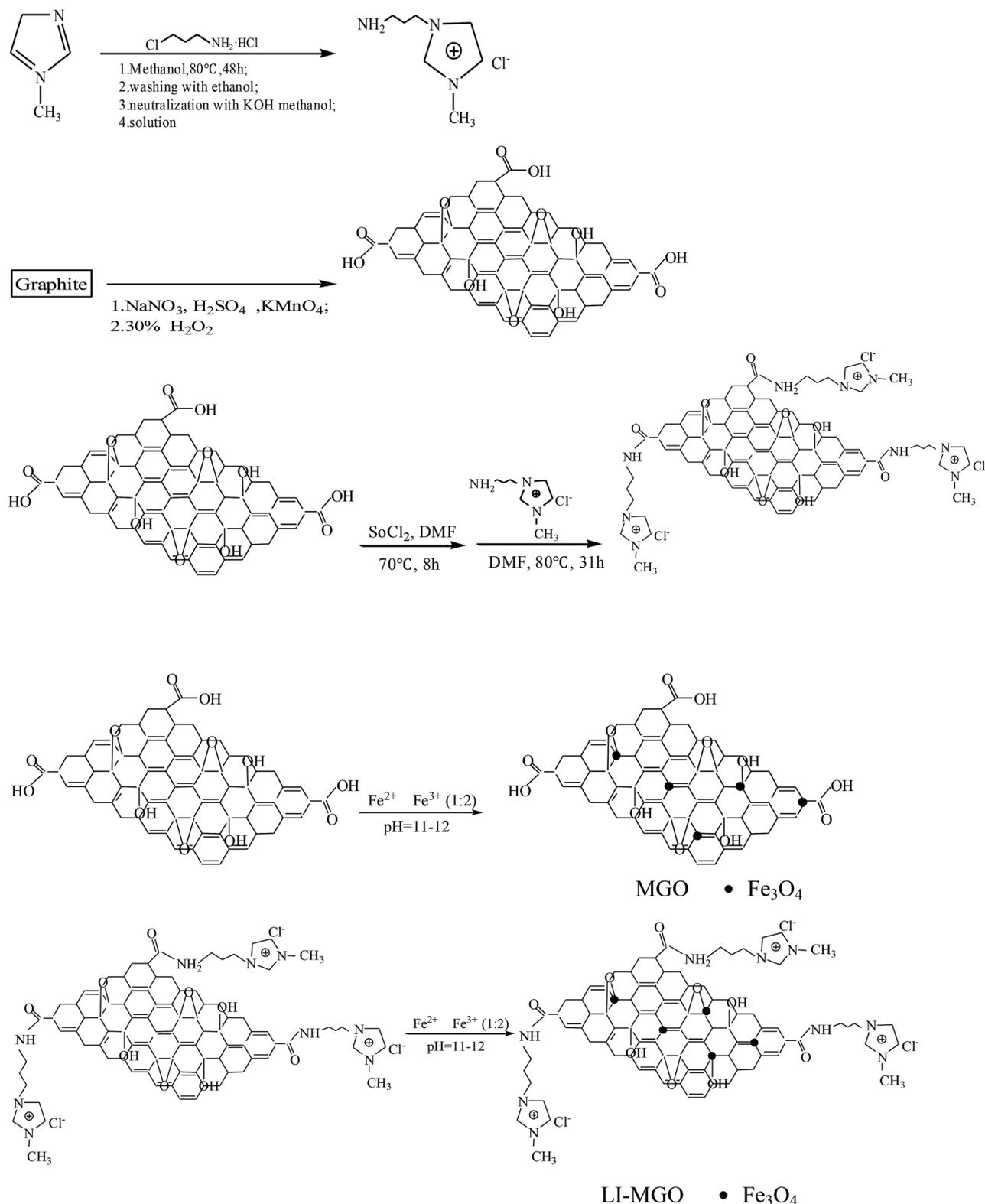Fig. 2 ^{1}H NMR spectrum of 1-amine-3-methyl imidazole chloride.

Fig. 3 Synthesis process of LI-MGO.

characteristic peak of the O–H stretching vibration, and the peak at 1690 cm^{-1} corresponds to C=O stretching vibrations of the –COOH groups. In the FTIR pattern of MGO, a strong adsorption band at 591 cm^{-1} was observed which was assigned to Fe–O

vibrations;[43] the characteristic peak from Fe–O vibration was also found in the FTIR pattern of LI-MGO. This revealed that Fe$_3$O$_4$ nanoparticles were effectively decorated on the surface of the GO layers. It is found that absorption bands at 1170 cm^{-1} and 1460
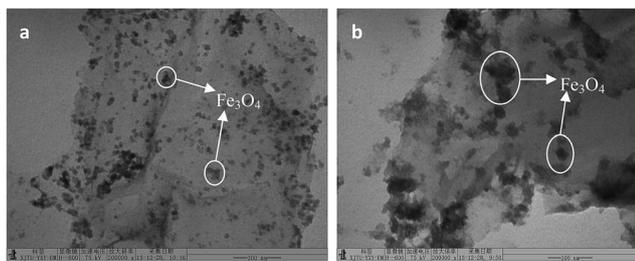
Fig. 4 TEM images of MGO (a) and LI-MGO (b).

Fig. 6 XRD patterns of GO (a), MGO (b) and LI-MGO (c).

cm^{-1} both emerged in the FT-IR spectra of LI-MGO and LI, which were attributed to C–N and C=C stretching vibrations, respectively. This indicated that LI has been added onto the MGO sheets.

In order to further study the chemical compositions of LI-MGO, GO, MGO and LI-MGO, they were analyzed using XRD as shown in Fig. 6. From Fig. 6a, a strong peak is shown at 11.43° that resulted from the (002) plane of GO, and a weak wide peak is shown at 21.62°, which is due to the presence of abundant oxygen-containing functional groups on GO and is similar to the reported value for graphite oxide.[44] As shown in Fig. 6b and c, six characteristic diffraction peaks appear at 2θ values of 30.2°, 35.6°, 43.3°, 53.7°, 57.1° and 62.8° in the XRD patterns of MGO and LI-MGO, which correspond to the (220), (311), (400), (422), (511) and (440) crystal planes of Fe_3O_4, respectively (JCPDS card: 019-0629). The diffraction peaks from Fe_3O_4 in the XRD pattern of LI-MGO are stronger than those in the pattern of MGO, but the diffraction peaks from GO were not found in the diffraction patterns of MGO and LI-MGO. The Wang[45] group also found the peaks from GO missing, and they attributed this phenomenon to two possible reasons. Firstly, as graphene oxide sheet layer aggregation is reduced due to the presence of magnetite, more single layer graphene oxide appears, so in the diffraction pattern the carbon diffraction peak appears as weak. The second reason is that the strong diffraction peak signals from iron oxide weaken the diffraction signal from carbon.

In addition, the specific surface areas of MGO and LI-MGO were examined using N_2 physisorption at −196 °C. Representative N_2 adsorption/desorption isotherms for such samples are shown in Fig. 7. Obviously, the isotherms for MGO and LI-MGO
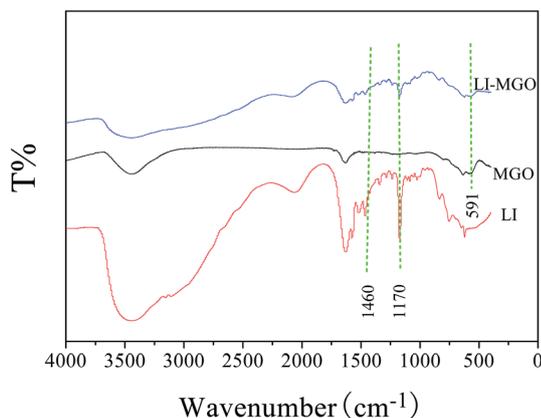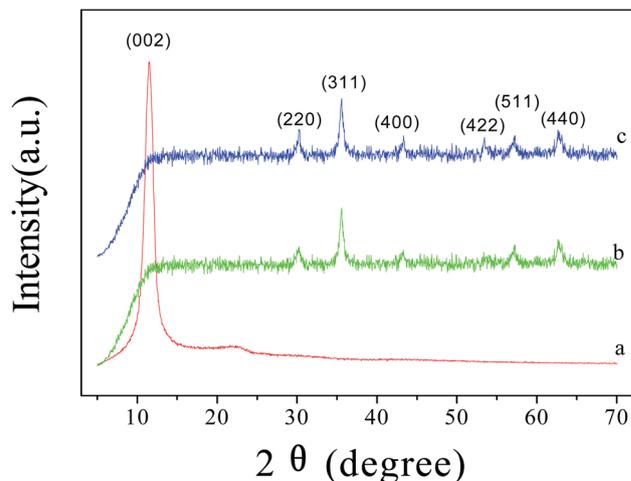
displayed similar features to a type IV isotherm, according to the IUPAC classification. The BET surface area and BJH cumulative pore volume of MGO were measured to be 64.20 m^2 g^{-1} and 0.2492 cm^3 g^{-1}, respectively. The BET surface area and BJH cumulative pore volume of LI-MGO were measured to be 110.3 m^2 g^{-1} and 0.2848 cm^3 g^{-1}, respectively. The BET surface area of LI-MGO is larger than MGO due to the surface of LI-MGO being rougher than MGO, after MGO was modified using LI, which is also seen in the TEM images for MGO and LI-MGO (Fig. 4).

3.2 Effect of pH on the adsorption capacity

pH is one of the important factors that affect adsorption performance. The effect of pH on the adsorption capacity for the four dyes is shown in Fig. 8. As illustrated in Fig. 8a, the adsorption capacity for GR on MGO and LI-MGO increases over the pH range from 2.0 to 3.0, while the adsorption capacity for GR on MGO decreases over the pH range from 3.0 to 7.0. However,
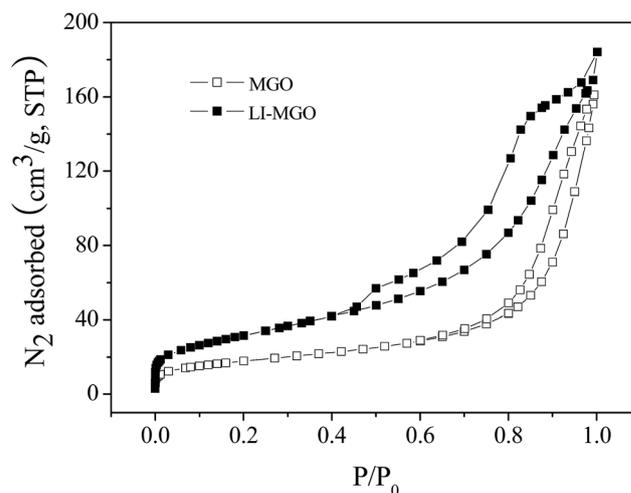

Fig. 5 FTIR spectra of LI, MGO and LI-MGO.

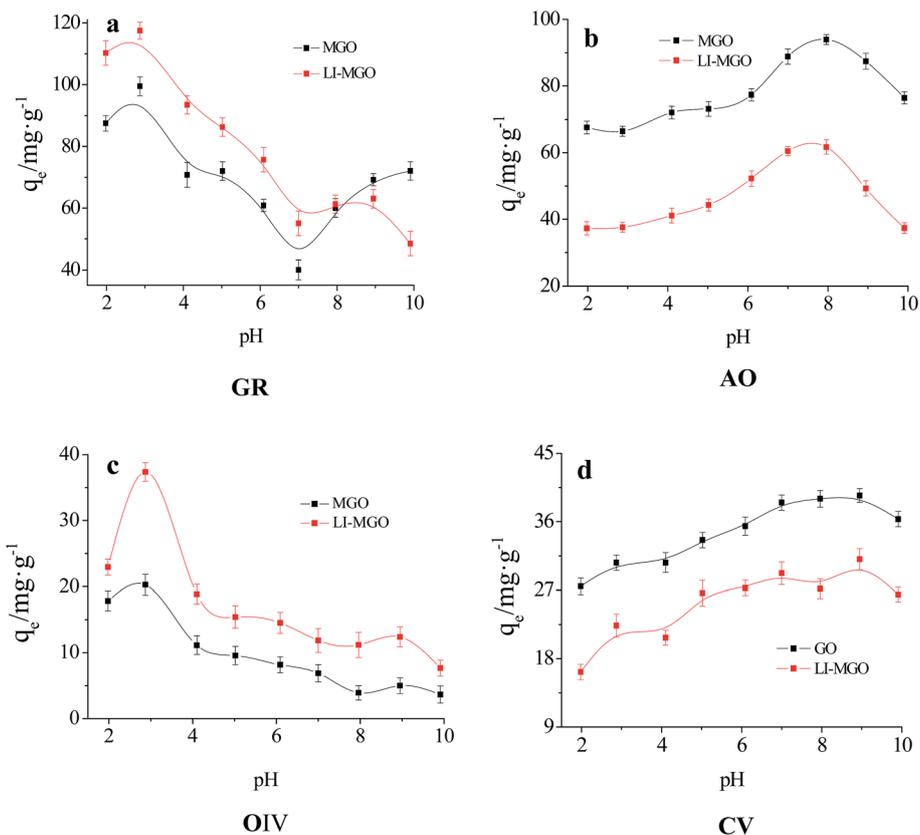Fig. 7 Nitrogen adsorption–desorption isotherms for MGO and LI-MGO.

Fig. 8 Effect of pH values on the adsorption capacities of MGO and LI-MGO: (a) GR; (b) AO; (c) OIV; and (d) CV.

when the pH is greater than 7.0, the adsorption capacity for GR on MGO increases gradually. The adsorption capacity for GR on LI-MGO decreases over the pH range from 3.0 to 10.0. The adsorption capacities for GR on MGO and LI-MGO both reach maximum values when the pH is 3.0. Fig. 8c shows that the adsorption capacity for OIV on MGO and LI-MGO is relatively lower at a low pH, such as pH 2.0, and the adsorption capacities for OIV on MGO and LI-MGO both reach a maximum at pH 3.0; then the adsorption capacity for OIV on MGO and LI-MGO gradually decreases with an increase in pH. As shown in Fig. 8b and d, the adsorption capacity for AO and CV increases along with an increase in pH. The adsorption capacity for AO reaches a maximum at pH 8.0, while the adsorption capacity for CV reaches a maximum at pH 9.0. Based on the experimental results, the most favorable pH values for GR, OIV, AO and CV adsorption on MGO and LI-MGO are around 3.0, 3.0, 8.0, and 9.0, respectively.

The effect of pH on adsorption capacity is not only related to the surface charge of the adsorbent, but also to the dissociated form of the dye. The zeta potentials of MGO and LI-MGO at different pH values are shown in Fig. 9. The zero potential points (pH$_{pzc}$) of MGO and LI-MGO are 2.4 and 2.9, respectively (Fig. 9). When the pH < 2.4, the surface of MGO is positively charged, while when the pH > 2.4, the surface of MGO is negatively charged. When the pH < 2.9, the surface of LI-MGO is positively charged, while when the pH > 2.9, the surface of LI-MGO is negatively charged. The four dyes include two anionic dyes, GR and OIV, and two cationic dyes, AO and CV. GR and OIV can exist

as anions when the pH > pK_a; the negative charge on the surface of MGO and LI-MGO at around pH 3.0 is lower and close to zero, so the electrostatic interaction between GR and OIV and MGO and LI-MGO is strongest, and the adsorption capacity is maximal. AO and CV can existed as cations when the pH > pK_a, and the negative charge on the surface of MGO and LI-MGO at around pH 8.0 is greatest. So the electrostatic interaction between AO and CV and MGO and LI-MGO is strongest, and the adsorption capacity reaches the maximum. In addition, the surface negative charge of
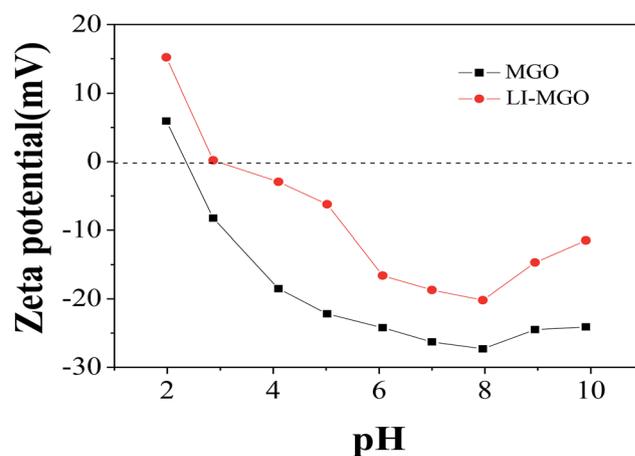

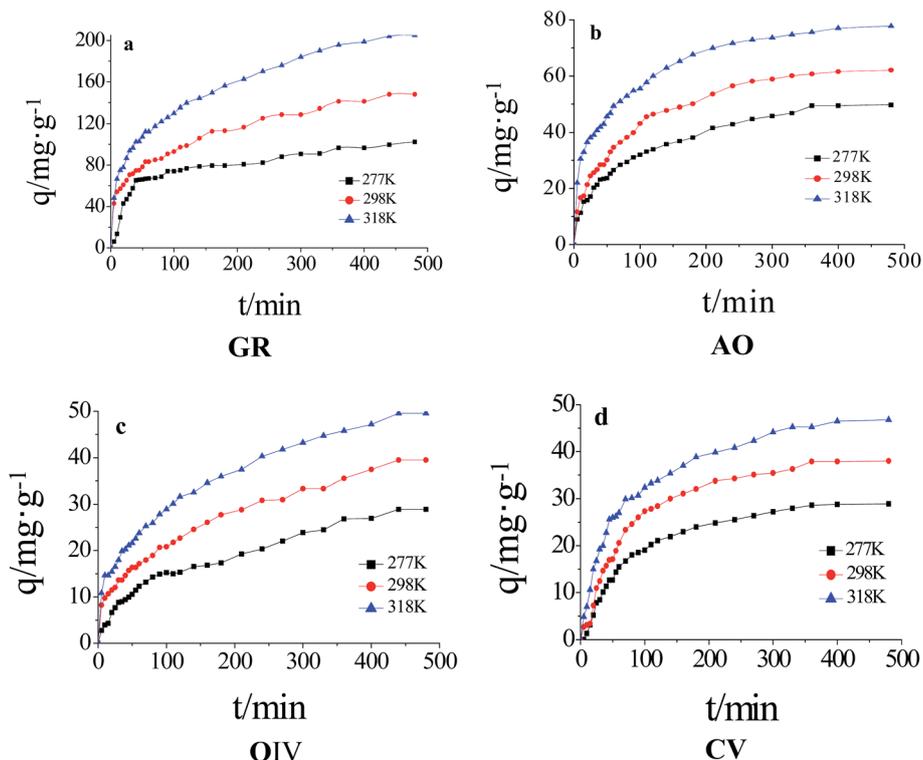**Fig. 9** Zeta potentials of MGO and LI-MGO at different pH values.

Fig. 10 Kinetics of dye adsorption on LI-MGO at 277 K, 298 K and 318 K: (a) GR; (b) AO; (c) OIV; (d) CV.

MGO is stronger than LI-MGO at different pH values (Fig. 9). This also can explain why the adsorption capacity for anionic dyes on LI-MGO is greater than on MGO and why the adsorption capacity for cationic dyes on MGO is greater than on LI-MGO.

3.3 Adsorption kinetics

Fig. 10 describes the adsorption capacity for four dyes on LI-MGO *versus* time at 277 K, 298 K and 318 K. The four dyes are adsorbed rapidly over the first 100 min, and thereafter they proceed at a slow rate and finally achieve equilibrium at 300 min. The adsorption capacity at equilibrium for the four dyes on LI-MGO increases as the temperature increases.

In order to study the mechanism of adsorption, the kinetic data were fitted using a pseudo-first-order kinetic model,[46] pseudo-second-order kinetic model[47] and intraparticle diffusion model;[48] the three models are expressed using the following equations:

$$\log(q_e - q_t) = \log q_e - k_1 \frac{t}{2.303} \qquad (2)$$

$$\frac{t}{q_t} = \frac{1}{k_2 q_e^2} + \frac{t}{q_e} \qquad (3)$$

$$q_t = k_{int} t^{1/2} \qquad (4)$$

Table 1 Kinetic parameters for the adsorption of dyes onto LI-MGO at 277 K, 298 K and 318 K

| Dye	T/K	q_{eqex}/mg g^{-1}	Pseudo-first-order kinetics model			Pseudo-second-order kinetics model			Intraparticle diffusion model	
			k_1 ($\times 10$ min^{-1})	q_e/mg g^{-1}	R^2	k_2 ($\times 10^2$ g mg^{-1} min^{-1})	q_e/mg g^{-1}	R^2	k_{int} (mg g^{-1} min$^{-1/2}$)	R^2
GR	277	102.2	0.0709	65.31	0.763	0.02138	106.4	0.988	3.960	0.806
	298	147.8	0.0613	100.23	0.929	0.01320	156.3	0.986	5.647	0.952
	318	204.9	0.0627	143.22	0.936	0.00897	217.9	0.986	8.159	0.958
	277	28.90	0.0497	24.39	0.909	0.02790	33.3	0.962	1.318	0.987
OIV	298	39.46	0.0557	31.94	0.967	0.02824	43.47	0.969	1.694	0.991
	318	49.59	0.0617	38.84	0.963	0.02547	55.56	0.980	2.111	0.983
	277	49.74	0.0778	39.40	0.957	0.03157	54.44	0.987	2.741	0.978
AO	298	62.08	0.0937	50.45	0.974	0.02720	68.63	0.992	3.763	0.979
	318	77.81	0.0942	54.14	0.953	0.03449	81.97	0.994	4.196	0.945
	277	28.84	0.0814	26.01	0.986	0.03523	34.78	0.998	2.789	0.989
CV	298	37.88	0.0947	32.70	0.978	0.03147	44.68	0.997	3.616	0.976
	318	46.46	0.0859	36.10	0.972	0.03419	51.89	0.996	3.894	0.967
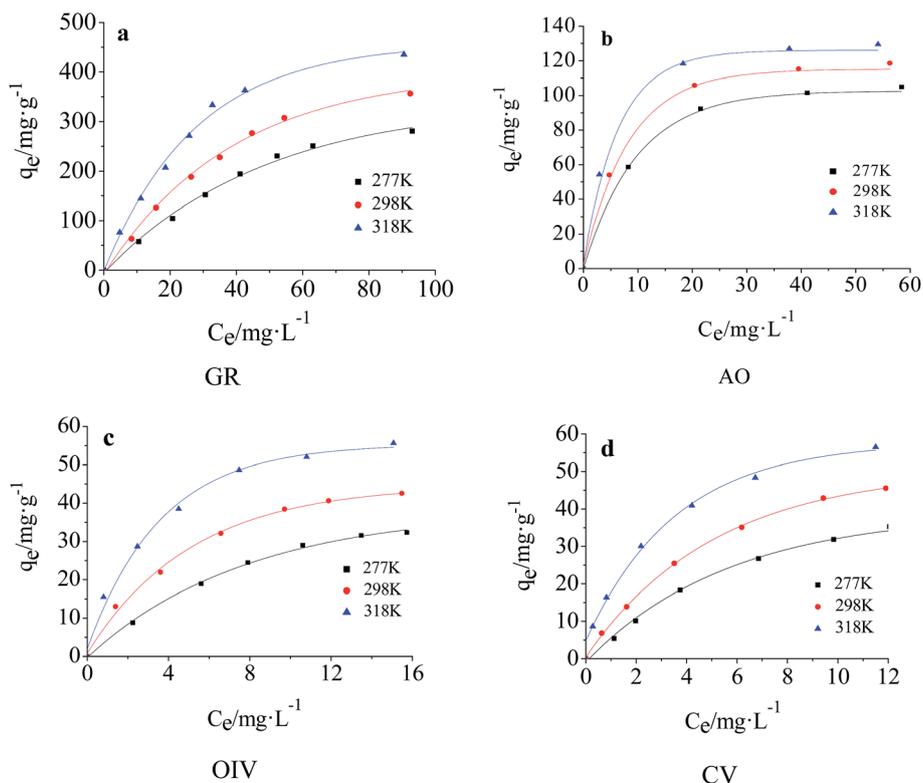
Fig. 11 Adsorption isotherms for dye adsorption on LI-MGO at 277 K, 298 K and 318 K: (a) GR; (b) AO; (c) OIV; (d) CV.

where q_e (mg g^{-1}) is the equilibrium adsorption capacity, q_t (mg g^{-1}) is the amount adsorbed at time t, k_1 is the equilibrium rate constant of pseudo-first-order adsorption (min^{-1}), k_2 (g mg^{-1} min^{-1}) is the rate constant of pseudo-second-order adsorption, and k_{int} (mg g^{-1} min$^{-1/2}$) is the rate constant for intraparticle diffusion adsorption.

k_1 and q_e were obtained from the slope and intercept of $\log(q_e - q_t)$ versus t, k_2 and q_e were obtained from the slope and intercept of t/q_t versus t, and k_{int} can be calculated from the slope of q_t versus $t_{0.5}$.

The kinetic parameters obtained from the pseudo-first-order equation, pseudo-second-order equation and intraparticle diffusion equation are listed in Table 1. The R^2 values and the large discrepancy between the experimental and calculated q_e indicates that the adsorption of the four dyes does not follow the pseudo first-order kinetic model or intraparticle diffusion model. As a result, the adsorption of the four dyes onto LI-MGO is in accordance with the pseudo second-order kinetic model, in which the adsorption process is the rate-limiting step, involving the surface.

3.4 Adsorption isotherms

The adsorption isotherms for OIV, GR, AO and CV on LI-MGO at 277 K, 298 K and 318 K are shown in Fig. 11. The adsorption capacity of LI-MGO reaches a maximum with an increase in initial dye concentration, as shown in Fig. 11.

The study of adsorption equilibrium can be a good assessment of adsorption capacity. The adsorption data for the dyes on LI-MGO were fitted using two classical adsorption models –

the Langmuir and Freundlich models. The Langmuir equation and Freundlich equation can be expressed in linear form using eqn (5) and (6), respectively.

$$\frac{C_e}{q_e} = \frac{1}{q_m K_L} + \frac{C_e}{q_m} \qquad (5)$$

$$\log q_e = \log K_F + \left[\frac{1}{n}\right] \log C_e \qquad (6)$$

where q_e and q_m (mg g^{-1}) are the dye adsorption capacity at equilibrium and the maximum adsorption capacity, respectively, K_L (L mg^{-1}) is the Langmuir constant, K_F

Table 2 Adsorption isotherm parameters for the adsorption of dyes onto LI-MGO at 277 K, 298 K and 318 K

Dye	T/K	Langmuir equation			Freundlich equation		
		q_m/mg g^{-1}	K_L/L mg^{-1}	R	K_F/mg g^{-1}	n	R
GR	277	578.03	0.01137	0.9778	9.9136	1.2835	0.9709
	298	588.24	0.01809	0.9907	15.541	1.3600	0.9792
	318	606.06	0.03080	0.9921	33.204	1.6273	0.9713
OIV	277	55.52	0.09538	0.9934	5.3265	1.4269	0.9902
	298	57.37	0.1947	0.9969	11.385	1.9495	0.9925
	318	65.65	0.3446	0.9988	19.136	2.5103	0.9697
AO	277	119.33	0.1328	0.9990	33.059	3.3436	0.9547
	298	132.80	0.1615	0.9994	34.103	3.0276	0.9646
	318	140.06	0.2449	0.9997	41.006	3.2066	0.9653
CV	277	65.96	0.09632	0.9958	6.2395	1.3786	0.9942
	298	69.44	0.1642	0.9983	9.9234	1.5185	0.9938
	318	70.03	0.3485	0.9994	18.001	1.9319	0.9928

Table 3 Thermodynamic parameters for the adsorption of four dyes onto LI-MGO

Dye	T/K	ΔG (kJ mol^{-1})	ΔH (kJ mol^{-1})	ΔS (J mol^{-1} K^{-1})
GR	277	−3.685	17.12	74.98
	298	−5.148		
	318	−6.771		
OIV	277	−3.354		
	298	−4.078	7.287	38.33
	318	−4.935		
AO	277	−1.959		
	298	−3.046	12.88	53.52
	318	−4.157		
CV	277	−2.469		
	298	−3.323	0.9550	42.34
	318	−4.209		

(mg mg^{-1}) is related to the adsorption capacity of the adsorbent, and $1/n$ is a constant that is related to adsorption intensity.

As shown in Table 2, the R value from the Langmuir model is much larger than that from the Freundlich isotherm, and the adsorption capacity calculated from the Langmuir isotherm is closer to the experimental q_e. Hence, the Langmuir model is more appropriate than the Freundlich model for describing the adsorption behavior of OIV, GR, AO and CV onto LI-MGO. This implies monolayer coverage of OIV, GR, AO and CV on LI-MGO and also a homogeneous distribution of active sites on the adsorbent, as the Langmuir equation assumes that the surface is homogeneous.

3.5 Adsorption thermodynamics

Thermodynamic parameter changes, such as in the standard free energy ($\Delta G°$/kJ mol^{-1}), enthalpy ($\Delta H°$/kJ mol^{-1}) and entropy ($\Delta S°$/J mol^{-1} K^{-1}), were calculated using the following equations:

$$\Delta G° = -RT \ln K_C \tag{7}$$

$$\Delta H° = \Delta G° + T\Delta S° \tag{8}$$

$$K_C = \frac{q_e}{C_e} \tag{9}$$

where K_C is the equilibrium constant. The van't Hoff equation is written as follows according to a combination of eqn (7), (8) and (9).

$$\ln K_C = \frac{-\Delta H°}{R}\frac{1}{T} + \frac{\Delta S°}{R}$$

$\Delta H°$ and $\Delta S°$ were calculated from the slope and intercept of a linear plot of $\ln K_C$ versus $1/T$ (Fig. S3, ESI†). The values of $\Delta G°$, $\Delta H°$ and $\Delta S°$ are listed in Table 3. The negative values of $\Delta G°$ indicate that adsorption is spontaneous at the studied temperatures. The positive values of $\Delta H°$ and $\Delta S°$ for the adsorption of the four dyes onto LI-MGO indicate that the adsorption process is endothermic and random, respectively. This also explains why the adsorption capacity at equilibrium for the four dyes on LI-MGO increases as the temperature increases.

3.6 Adsorption capacity comparison

A comparison of adsorbents from similar anionic dye studies reported in the literature is displayed in Table 4. The maximum adsorption capacity of glenn black R on LI-MGO is greater compared to other anionic dyes on absorbents reported in the literature. LI-MGO has superior adsorption efficiency for anionic dyes, which may be ascribed to the surface of MGO having increased positive charge after 1-amine-3-methyl imidazole chloride functionalization.

Table 4 Comparison of the maximum adsorption capacities for anionic dyes of different adsorbents

Adsorbent	Anionic dye	Maximum adsorption capacity (mg g^{-1})	Reference
Fe$_3$O$_4$@nSiO$_2$@mSiO$_2$@DHIM-NH$_2$	Orange II	142.49	49
NMC-3-800	Amaranth	79.84	50
	Methyl orange	202.4	
GG-g-poly(DMAEMA) gels	Methyl orange	25.8	51
CTAB-modified pumice	Congo red	27.32	52
HCPZA	Eriochrome black T	15.9	53
Fe$_3$O$_4$@GPTMS@P-Lys	Orange I	104.36	54
	Amaranth	84.04	
	Acid red 18	134.69	
PbO-NP-AC	Methyl orange	333.33	55
CMOPP	Congo red	163	56
Amine/Fe$_3$O$_4$-resin	Methyl orange	101.0	57
	Reactive brilliant red K-2BP	222.2	
	Acid red 18	99.4	
Fe$_3$O$_4$/MIL-101(Cr)	Acid red 1	142.9	58
	Orange G	200.0	
LI-MGO	glenn black R	588.24	This work
	orange IV	57.37	

4 Conclusions

In summary, a novel LI-MGO adsorbent functionalized with 1-amine-3-methyl imidazole chloride ionic liquid was successfully prepared through a facile chemical co-precipitation and chemical modification method. LI-MGO exhibited a higher surface area than MGO. In order to research the adsorption properties of LI-MGO, two kinds of anionic dyes, OIV and GR, and two kinds of cationic dyes, AO and CV, were investigated as model dyes. LI-MGO showed remarkably higher adsorption capacities for the anionic dyes compared with MGO and referenced materials, due to LI-MGO being a surface cationic modified material and electrostatic interactions between LI-MGO and the anionic dyes. In addition, the advantages of its rapid separation from water and low cost give LI-MGO a good chance to be applied in the removal of anionic dyes from wastewater.

Conflict of interest

The authors declare there is no conflict of interest.

Acknowledgements

References

1 K. R. Ramakrishna and T. Viraraghavan, *Water Sci. Technol.*, 1997, **36**, 189–196.
2 N. R. Khalid, E. Ahmed, Z. Hong, L. Sana and M. Ahmed, *Curr. Appl. Phys*, 2013, **13**, 659–663.
3 D. Stergiopoulos, K. Dermentzis, P. Giannakoudakis and S. Sotiropoulos, *Global NEST J.*, 2014, **16**, 499–506.
4 M. F. Abid, M. A. Zablouk and A. M. Abidalameer, *Iran. J. Environ. Health Sci. Eng.*, 2012, **9**, 17–25.
5 M. Wawrzkiewicz, *Chem. Eng. J.*, 2013, **217**, 414–425.
6 T. Ma, P. R. Chang, P. Zheng, F. Zhao and X. Ma, *Chem. Eng. J.*, 2014, **240**, 595–600.
7 N. Öztürk and T. E. Bektas, *Fresenius Environ. Bull.*, 2006, **15**, 489–496.
8 W. Hajjaji, R. C. Pullar, J. A. Labrincha and F. Rocha, *Appl. Clay Sci.*, 2016, **126**, 197–206.
9 S. Yang, L. Wang, X. Zhang, W. Yang and G. Song, *Chem. Eng. J.*, 2015, **275**, 315–321.
10 L. Gao, Q. Li, X. Hu, X. Wang, H. Song, L. Yan and H. Xiao, *Appl. Clay Sci.*, 2016, **126**, 299–305.
11 Y. Yu, B. N. Murthy, J. G. Shapter, K. T. Constantopoulos, N. H. Voelcker and A. V. Ellis, *J. Hazard. Mater.*, 2013, **260**, 330–338.
12 H. Gao, Y. Sun, J. Zhou, R. Xu and H. Duan, *ACS Appl. Mater. Interfaces*, 2013, **5**, 425–432.
13 M. S. Mauter and M. Elimelech, *Environ. Sci. Technol.*, 2008, **42**, 5843–5859.
14 J. Liu, W. Liu, Y. Wang, M. Xu and B. Wang, *Appl. Surf. Sci.*, 2016, **367**, 327–334.
15 D. Robati, B. Mirza, M. Rajabi, O. Moradi, I. Tyagi, S. Agarwal and V. K. Gupta, *Chem. Eng. J.*, 2016, **284**, 687–697.
16 D. Wang, L. Liu, X. Jiang, J. Yu, X. Chen and X. Chen, *Appl. Surf. Sci.*, 2015, **329**, 197–205.
17 S. T. Yang, S. Chen, Y. Chang, A. Cao, Y. Liu and H. Wang, *J. Colloid Interface Sci.*, 2011, **359**, 24–29.
18 G. Xie, P. Xi, H. Liu, F. Chen, L. Huang, Y. Shi, *et al.*, *J. Mater. Chem.*, 2012, **22**, 1033–1039.
19 V. K. Sharma, T. J. Mcdonald, H. Kim and V. K. Garg, *Adv. Colloid Interface Sci.*, 2015, **225**, 229–240.
20 O. Moradi, V. K. Gupta, S. Agarwal, I. Tyagi, M. Asif, *et al.*, *J. Ind. Eng. Chem.*, 2015, **28**, 294–301.
21 J. Liu, G. Liu and W. Liu, *Chem. Eng. J.*, 2014, **257**, 299–308.
22 D. Wang, L. Liu, X. Jiang, J. Yu and X. Chen, *Colloids Surf., A*, 2015, **466**, 166–173.
23 R. Rajesh, S. S. Iyer, J. Ezhilan, S. S. Kumar and R. Venkatesan, *Spectrochim. Acta, Part A*, 2016, **166**, 49–55.
24 H. Wang, H. Gao, M. Chen, X. Xu, X. Wang, *et al.*, *Appl. Surf. Sci.*, 2016, **360**, 840–848.
25 D. Chen, H. Zhang, K. Yang and H. Wang, *J. Hazard. Mater.*, 2016, **310**, 179–187.
26 P. N. Diagboya, B. I. Olu-Owolabi, D. Zhou and B. H. Han, *Carbon*, 2014, **79**, 174–182.
27 G. K. Ramesha, A. V. Kumara, H. B. Muralidhara and S. Sampath, *J. Colloid Interface Sci.*, 2011, **361**, 270–277.
28 T. Zhou, W. Lu, L. Liu, H. Zhu, Y. Jiao, S. Zhang and R. Han, *J. Mol. Liq.*, 2015, **211**, 909–914.
29 C. Namasivayam and M. V. Sureshkumar, *J. Appl. Polym. Sci.*, 2006, **100**, 1538–1546.
30 Y. Su, B. Zhao, W. Xiao and R. Han, *Environ. Sci. Pollut. Res.*, 2013, **20**, 5558–5568.
31 V. S. Munagapati and D. S. Kim, *J. Mol. Liq.*, 2016, **220**, 540–548.
32 K. Li, P. Li, J. Cai, S. Xiao, H. Yang and A. Li, *Chemosphere*, 2016, **154**, 310–318.
33 M. Armand, F. Endres, D. R. Macfarlane, H. Ohno and B. Scrosati, *Nat. Mater.*, 2009, **8**, 621–629.
34 N. V. Plechkova and K. R. Seddon, *Chem. Soc. Rev.*, 2008, **37**, 123–150.
35 U. Domańska, P. Okuniewska and M. Królikowski, *Fluid Phase Equilib.*, 2016, **423**, 109–119.
36 B. Lam, M. Wei, L. Zhu, S. J. Luo, R. Guo, *et al.*, *Polymer*, 2016, **89**, 1–11.
37 K. Moodley, M. Mabaso, I. Bahadur and G. G. Redhi, *J. Mol. Liq.*, 2016, **219**, 206–210.
38 B. Lin, H. Shang, F. Chu, Y. Ren, N. Yuan, B. Jia, *et al.*, *Electrochim. Acta*, 2014, **134**, 209–214.
39 Q. Zhou, F. Chen, W. Wu, R. Bu, W. Li and F. Yang, *Chem. Eng. J.*, 2016, **285**, 198–206.
40 W. Song, Y. Liu, L. Qian, L. Niu, L. Xiao, *et al.*, *Chem. Eng. J.*, 2016, **287**, 482–491.
41 L. X. Gao and J. Yu, *Chem. J. Chin. Univ.*, 2013, **34**, 108–114.
42 L. Sun, H. Yu and B. Fugetsu, *J. Hazard. Mater.*, 2012, **203–204**, 101–110.
43 F. Bianchi, F. Chiesi, F. Casoli, P. Luches, L. Nasi, M. Careri and A. Mangia, *J. Chromatogr. A*, 2012, **1231**, 8–15.
44 P. Bradder, S. K. Ling, S. Wang and S. Liu, *J. Chem. Eng. Data*, 2011, **56**, 138–141.

45 X. Yang, C. Chen, J. Li, G. Zhao, X. Ren and X. Wang, *RSC Adv.*, 2012, **2**, 8821–8826.

46 A. Aluigi, F. Rombaldoni, C. Tonetti and L. Jannoke, *J. Hazard. Mater.*, 2014, **268**, 156–165.

47 Z. Chen, J. Zhang, J. Fu, M. Wang, X. Wang, R. Han and Q. Xu, *J. Hazard. Mater.*, 2014, **273**, 263–271.

48 S. Wan, F. He, J. Wu, W. Wan, Y. Gu and B. Gao, *J. Hazard. Mater.*, 2016, **314**, 32–40.

49 J. Cheng, L. Shi and J. Lu, *J. Ind. Eng. Chem.*, 2016, **36**, 206–214.

50 H. Li, N. An, G. Liu, J. Li, N. Liu, M. Jia, *et al.*, *J. Colloid Interface Sci.*, 2016, **466**, 343–351.

51 J. S. Karthika and B. Vishalakshi, *Int. J. Biol. Macromol.*, 2015, **81**, 648–655.

52 H. Shayesteh, A. Rahbar-Kelishami and R. Norouzbeigi, *J. Mol. Liq.*, 2016, **221**, 1–11.

53 T. A. Saleh, A. M. Muhammad and S. A. Ali, *J. Colloid Interface Sci.*, 2016, **468**, 324–333.

54 Y. R. Zhang, P. Su, J. Huang, Q. R. Wang and B. X. Zhao, *Chem. Eng. J.*, 2015, **262**, 313–318.

55 M. Ghaedia, A. M. Ghaedi, B. Mirtamizdoust, S. Agarwal and V. K. Gupta, *J. Mol. Liq.*, 2016, **213**, 48–57.

56 V. S. Munagapati and D. S. Kim, *J. Mol. Liq.*, 2016, **220**, 540–548.

57 W. Song, B. Gao, X. Xu, L. Xing, S. Han, *et al.*, *Bioresour. Technol.*, 2016, **210**, 123–130.

58 T. Wang, P. Zhao, N. Lu, H. Chen, *et al.*, *Chem. Eng. J.*, 2016, **295**, 403–413.